

Differentiating Between Cancer and Inflammation: A Metabolic-Based Method for Functional Computed Tomography Imaging

Menachem Motiei,^{†,#} Tamar Dreifuss,^{†,#} Oshra Betzer,[†] Hana Panet,[†] Aron Popovtzer,[‡] Jordan Santana,[†] Galith Abourbeh,^{||} Eyal Mishani,^{||} and Rachela Popovtzer^{*,†}

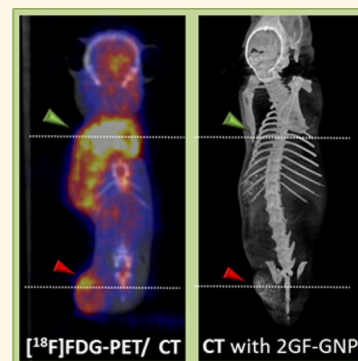
[†]Faculty of Engineering and the Institutes of Nanotechnology & Advanced Materials, Bar-Ilan University, Ramat-Gan 5290002, Israel

[‡]Davidoff Cancer Center, Rabin Medical Center, Beilinson Campus, Petah Tiqva 4941492, Israel

^{||}Cyclotron-Radiochemistry-MicroPET Unit, Hadassah-Hebrew University Hospital, Jerusalem 91120, Israel

Supporting Information

ABSTRACT: One of the main limitations of the highly used cancer imaging technique, PET-CT, is its inability to distinguish between cancerous lesions and post treatment inflammatory conditions. The reason for this lack of specificity is that [¹⁸F]FDG-PET is based on increased glucose metabolic activity, which characterizes both cancerous tissues and inflammatory cells. To overcome this limitation, we developed a nanoparticle-based approach, utilizing glucose-functionalized gold nanoparticles (GF-GNPs) as a metabolically targeted CT contrast agent. Our approach demonstrates specific tumor targeting and has successfully distinguished between cancer and inflammatory processes in a combined tumor-inflammation mouse model, due to dissimilarities in angiogenesis occurring under different pathologic conditions. This study provides a set of capabilities in cancer detection, staging and follow-up, and can be applicable to a wide range of cancers that exhibit high metabolic activity.



KEYWORDS: cancer, FDG-PET, CT, gold nanoparticles, metabolic-based imaging

Cancer detection is based on both structural and functional imaging techniques. Structural techniques (e.g., US, MRI and CT) identify anatomic details and provide information on tumor location, size and spread, based on endogenous tissue contrast. However, they are not sufficiently sensitive for detecting critically small tumors or metastases since they lack structural manifestation. The development of the main clinically applicable functional imaging technique, positron emission tomography (PET) using the glucose analog ¹⁸F-2-fluoro-2-deoxy-D-glucose ([¹⁸F]FDG) has revolutionized the field of medical oncology. [¹⁸F]FDG-PET is based on the increased metabolic profile of malignant cells, and provides the ability to discern molecular and cellular alterations associated with pathological conditions, even before structural modifications occur. However, since there are biological processes other than cancer that exhibit increased glucose metabolic activity, such as infectious diseases or inflammatory conditions, high rates of false positive findings are reported in [¹⁸F]FDG-PET imaging.^{1,2} In addition, [¹⁸F]FDG-PET lacks anatomical information, and thus necessitates the incorporation of an additional structural imaging modality such as CT or MRI in order to obtain an accurate anatomic localization of the foci of increased metabolic activity. The combination of PET with CT (PET-CT) enables

both functional and anatomical information in a single setting. However, in view of the relatively high cost of PET scans, the dependence on the short-lived [¹⁸F]FDG ($T_{1/2} < 2$ h) and its nonspecificity for cancer, the development of a single modality which will overcome these drawbacks is highly desirable.

In the present work we demonstrate the development of a novel metabolic-based CT imaging technique using GF-GNPs, which provides simultaneous functional (metabolic) and structural imaging capabilities, with the most widely available imaging modality—the CT.

GNPs are ideal CT contrast agents,^{3–11} due to the relatively high X-ray attenuation of gold and the stability of gold colloids. In addition, GNPs are easy to synthesize, and their size and shape can be precisely controlled.^{11–15} Previous studies have revealed that GNPs are safe, as they caused minimal impairment of cell viability and functionality *in vitro*,^{16,17} and no evidence of toxicity has been observed for them *in vivo*.¹⁸

On the basis of previous knowledge that newly formed blood vessels in growing tumors differ from those in different pathologic conditions, including inflammation,¹⁹ we hypothe-

Received: December 1, 2015

Accepted: February 17, 2016

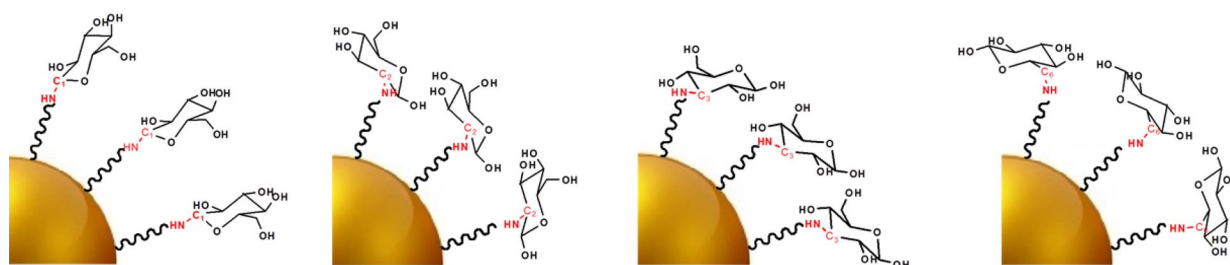


Figure 1. Schematic diagram of the four distinct GF-GNPs, with the same shape and size, differing only in the intramolecular glucose conjugation site (C_1 , C_2 , C_3 , and C_6).

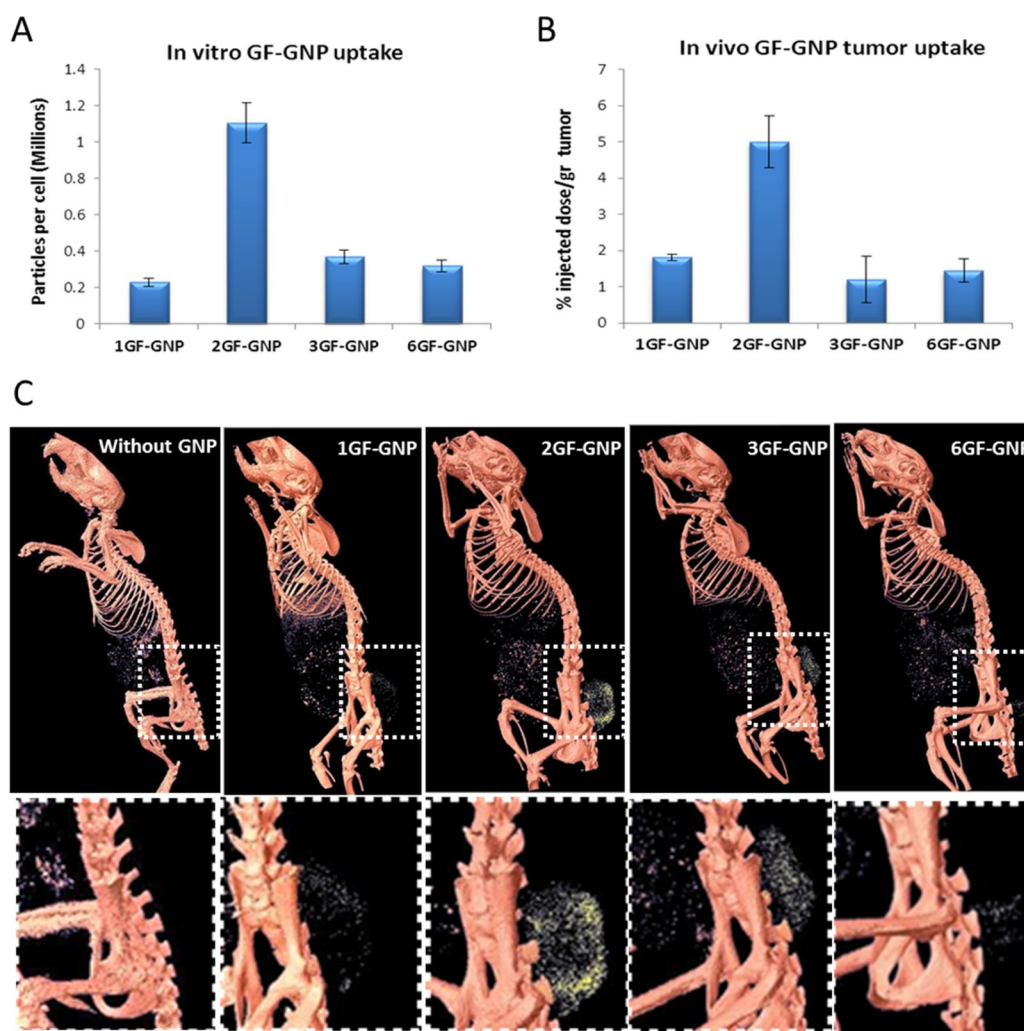


Figure 2. Selective uptake of 2GF-GNPs. (A) Cellular uptake of GF-GNPs into A431 SCC cell line, as measured by atomic absorption spectroscopy. Results presented as mean \pm SEM. Cancer cells demonstrate increased uptake while the glucose molecule is connected to the GNP through its 2' carbon position. (B) *In vivo* tumor uptake of GF-GNPs, as measured by atomic absorption spectroscopy. 2GF-GNP exhibits increased tumor uptake. Results presented as mean \pm SEM. (C) CT volume-rendered images of five mice; one without injection of nanoparticles (left), and four mice at 3.5 h post IV injection of the four types of GF-GNPs. Upper images: whole body volume-rendered images. The tumor area is marked with a white dashed rectangle. It is demonstrated that the tumor cannot be identified without injection of GNP (upper left image), while a significant accumulation of GNP can be observed following injection of 2GF-GNP. Some accumulation of GNP can be observed in the tumor area following injection of 1GF-GNP, 3GF-GNP and 6GF-GNP, which can be attributed to the passive targeting mechanism. For all mice, CT contrast is observed also in the digestive system due to food. In addition, in mice which were injected with GNPs, nanoparticles can be identified in the abdomen, as they accumulate in the kidneys, liver, and spleen according to their well-described clearance mechanism.^{49,50} Bottom images are enlarged images of the white marked tumor area.

sized that the proposed nanoparticle-based technique may provide the ability to differentiate tumors from nonmalignant metabolically active processes (inflammations and infections). Although both inflammatory lesions and tumor tissues exhibit

an enhanced permeability and retention (EPR) effect,^{20–23} tumor vasculatures have unique characteristics, as they are irregular in size, shape, and branching pattern.²⁴ In addition, they do not have a normal vascular hierarchy²⁵ and they exhibit

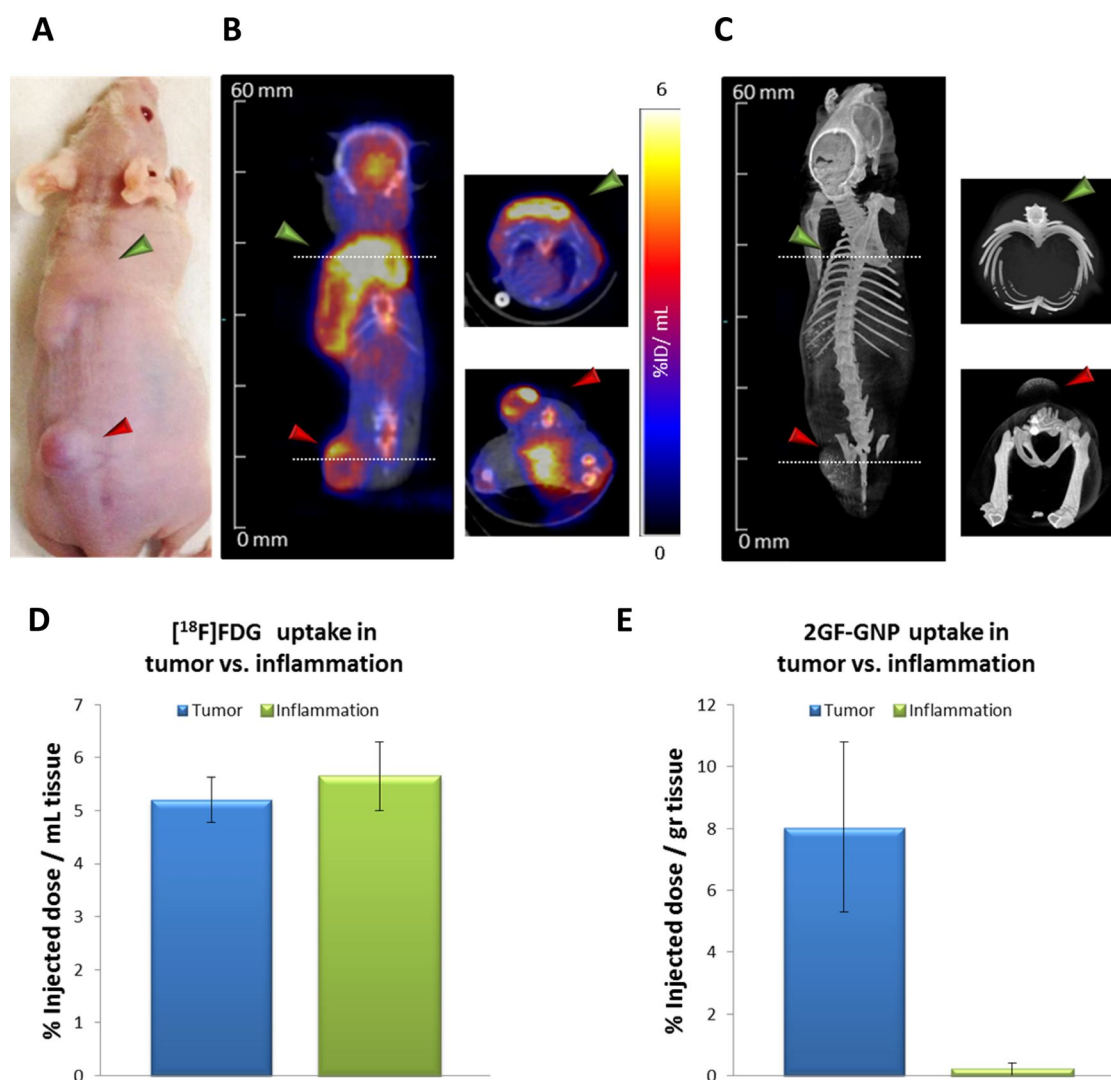


Figure 3. Differentiation between cancer and inflammation: Green arrowheads indicate location of inflammation; red arrowheads indicate location of A431 tumors. (A) Representative image of a combined tumor and inflammation mouse model, after 2GF-GNP injection. (B) [¹⁸F]FDG-PET/CT slice images of a representative mouse at 40–60 min post injection. [¹⁸F]FDG accumulates equally in both tumor and inflammation, and does not distinct between them. (C) CT surface-rendered images of the same mouse at 3.5 h post IV injection of 2GF-GNP. Gold accumulation is observed in the tumor, yet not in the inflammation, allowing a clear distinction between the two. (D) Quantification of [¹⁸F]FDG concentration in the tumor and inflammatory lesion. (E) Atomic absorption spectroscopy measurements of 2GF-GNP accumulation in tumor and inflammation. Results presented as mean ± SEM.

defects in endothelial cell barrier function, which enhance vessel leakiness.²⁶ Furthermore, while inflammation is characterized by increased blood flow and development of an expanded network of lymphatics, most blood vessels in tumors exhibit marginal blood flow and highly impaired lymphatic drainage, enabling retention of macromolecules in the tumor.^{19,27–32} These dissimilarities have led us to hypothesize that GF-GNPs may accumulate and retain in tumors to a greater extent than in inflammatory lesions, allowing a differentiation between the two. Indeed, our approach has demonstrated specific tumor targeting and has successfully distinguished between cancer and inflammatory processes in a combined tumor-inflammation mouse model.

RESULTS AND DISCUSSION

GF-GNP Synthesis and Characterization. First, we have synthesized four types of GF-GNPs, wherein the GNP was attached selectively to one of four possible intramolecular

glucosamine sites. The hydroxyl groups (–OH) of glucose can be substituted by amine groups (–NH₂) at different and specific molecular sites, denoted 1, 2, 3, or 6 (C-1, C-2, C-3 and C-6, respectively). Identically, 20 nm GNPs were synthesized and linked selectively to each of the 4 glucosamine sites, one at the time, resulting in four distinct GF-GNPs of the same shape and size, differing only in the intramolecular glucose site being functionalized (Figure 1). Twenty nanometer GNPs have been chosen due to their ability to accumulate in the tumor site^{33,34} as well as their biocompatibility and low toxicity.^{17,18} Characterization of the particles was performed using TEM, UV–vis spectroscopy, dynamic light scattering (DLS) and Zeta potential (Supplementary Figure S1).

In Vitro and In Vivo Evaluation of the Interaction between GF-GNPs and Cancer Cells. In order to examine the interaction between the GF-GNPs and cancer cells, we first performed an *in vitro* study, focusing on the question of whether the glucose molecule (~1 nm) retains some of its

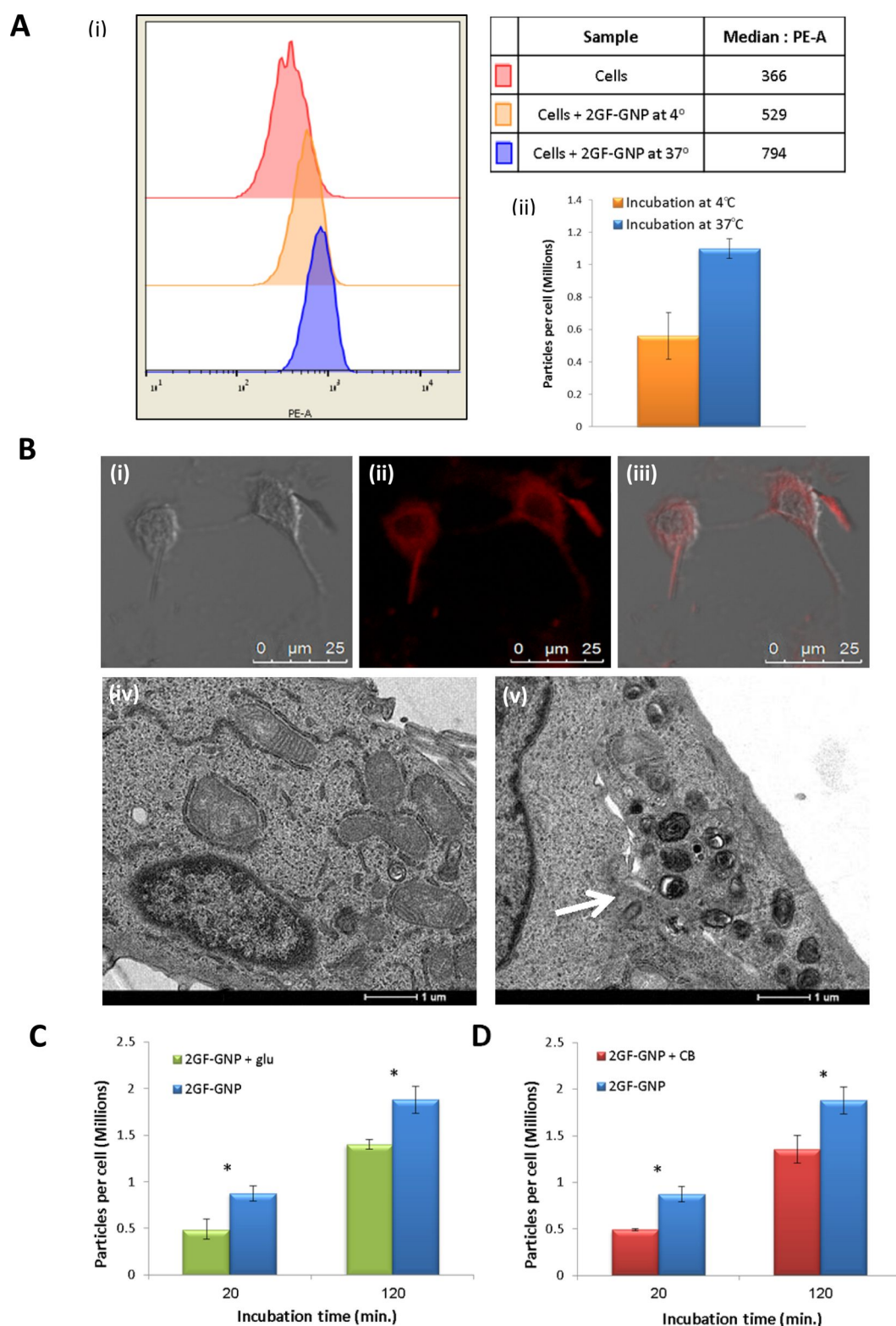


Figure 4. Internalization mechanism of 2GF-GNPs. (A) 2GF-GNPs internalization after incubation at 37 °C in comparison to 4 °C: (i) Representative histograms of GNP binding and uptake in cancer cells determined by flow cytometry (FACS). Red: control cancer cells (without GNPs); orange: cancer cells loaded with GNPs at 4 °C; blue: cancer cells loaded with GNPs at 37 °C. (ii) Atomic absorption spectroscopy measurements. 2GF-GNPs were internalized to a significantly lesser extent when kept at 4 °C compared to 37 °C. (B) (i–iii) Confocal images of A431 cells after 30 min incubation with Rhodamine B-2GF-GNP complex: (i) bright field image of the cells, (ii) fluorescent-coated 2GF-GNPs (red), (iii) combined images. (iv–v) TEM images of A431 cancer cells: (iv) A431 cells without GNPs, and (v) after 30 min incubation with 2GF-GNP. White arrow points at the accumulation of well-defined nanoparticles inside the endosome. (C) Saturation with free glucose: 2GF-GNP uptake after incubation with high glucose medium (10 mg/mL) was significantly lower than after incubation with normal glucose levels (4.5 mg/mL). (D) Cytochalasin B inhibition test: preincubation with CB has significantly inhibited the uptake of 2GF-GNP. Results presented as mean \pm SD (* p < 0.05 by t test).

activity and can be recognized as glucose by cells, when conjugated to a “large” GNP (20 nm). The four types of GF-GNPs were incubated with squamous cell carcinoma (SCC) human epidermoid A431 cancer cells ($n = 3$ per group) for 30 min, and atomic absorption spectroscopy was used to quantitatively determine the amount of internalized Au. Interestingly, despite their identical shapes and sizes, a significantly higher uptake was observed for the GNPs that were conjugated to glucose through its 2' carbon position (denoted as 2GF-GNP). The uptake was about 3 times greater than that of 3GF-GNP and 6GF-GNP, and about 5 times greater than that of 1GF-GNP (Figure 2A). In correlation with these quantitative results, confocal microscopy images have also showed higher cellular internalization for 2GF-GNP (Supplementary Figure S2). The same trend was observed also *in vivo*. GF-GNPs were intravenously (IV) injected into mice bearing human A431 tumors ($n = 5$ for each group), and gold concentration in the tumor was quantitatively measured by atomic absorption spectroscopy. Results showed that the uptake of 2GF-GNP was about 3 times greater than that of the other three GF-GNP conjugates (2.7, 3.8, and 2.9 times greater than 1GF-GNP, 3GF-GNP and 6GF-GNP, respectively) (Figure 2B). Given that the four nanoparticle types are of the same material (gold), coated by the same molecule (glucosamine) and have the same physicochemical characteristics, while differing only in the intramolecular glucose conjugation site, one would expect to obtain similar tumor uptake values of the four GNP types. Unexpectedly though, both *in vitro* and *in vivo* experiments showed a remarkably selective accumulation of one of the four isomer-conjugates. This difference in uptake provides evidence that the 2GF-GNPs are recognized and preferred by cancer cells, probably because of the specificity of the glucose coating. Interestingly, the 2' carbon position is also the one to which the ^{18}F is attached in [^{18}F]FDG, supporting our result that chemical modification of the 2' carbon position does not prevent glucose recognition by cells. In addition, it has been previously demonstrated that the 1', 3' and 6' carbon positions, as opposed to the 2' carbon position, are critically important in glucose binding to one of the major glucose transporters, GLUT-1.^{35,36} The differential uptake *in vivo* also underscores the distinction between passive targeting of the 1GF-GNP, 3GF-GNP and 6GF-GNP, which is due to the EPR effect, and metabolically active targeting of the 2GF-GNP.

In Vivo CT Experiments with Tumor Bearing Mice. CT scans of the tumor bearing mice which were IV injected with the GF-GNPs were performed preinjection and at 3.5 h postinjection of the GF-GNPs. The results markedly showed that the uptake of 2GF-GNP was significantly higher than that of the other three GF-GNP conjugates (Figure 2C). The mean density values within the tumors (range: 0–255, obtained by ImageJ) were 0.5 ± 0.1 , 23.5 ± 1.4 , 95.9 ± 3.7 , 51.6 ± 6.3 , 18.8 ± 4.5 , for mice without GNP injection, and after injection of 1GF-GNP, 2GF-GNP, 3GF-GNP and 6GF-GNP, respectively. In addition, it can be seen that small tumors (approximately 4–5 mm in diameter), which were undetectable by CT without the use of GNP contrast agents (Figure 2C, left image), became clearly visible and detectable following administration of 2GF-GNP, which like [^{18}F]FDG can detect glucose metabolic activity while inducing distinct contrast in CT imaging.

Evaluation of the Ability of 2GF-GNP to Differentiate between Cancer and Inflammation *In Vivo*. To evaluate the specificity of 2GF-GNPs for cancer, we compared the

abilities of 2GF-GNPs and of [^{18}F]FDG to differentiate A431 tumors from turpentine-induced inflammation in a combined tumor-inflammation mouse model. Inflammation was established in mice bearing A431 tumors ($n = 14$) by a subcutaneous injection of turpentine oil, and 4 days post turpentine injection, 2GF-GNP or [^{18}F]FDG were IV injected. It has been previously demonstrated that maximum uptake of [^{18}F]FDG occurs at 4 days post injection in this inflammation model,^{37,38} and therefore, this time point was selected for imaging. Subsequently, CT scans were performed at 3.5 h after 2GF-GNP injection, and after sacrifice, gold concentration in the tumor, in the inflammatory lesion and in the main organs were quantitatively measured by atomic absorption spectroscopy (Figure 3E and Supplementary Figure S3). Interestingly, both CT and atomic absorption spectroscopy results showed high-density accumulation of gold in the tumor, while practically no gold was detected in the inflammation region. The mean density values in the tumor and inflammation regions were 97.7 ± 1.0 and 1.6 ± 0.5 , respectively (obtained by ImageJ). For comparison, [^{18}F]FDG PET-CT scans were performed on four mice at 40–60 min after [^{18}F]FDG injection, showing no differentiation between cancer and inflammation, which exhibited equal accumulation of the radioactive tracer, with no visible nor quantitative differentiation between the two (Figure 3).

Cellular Study of the Internalization Mechanism of 2GF-GNPs. In order to reveal insights into the underlying mechanism that triggers the preferential uptake of 2GF-GNPs by tumors, we have performed an *in vitro* study with A431 cells. Since the uptake of both glucose and [^{18}F]FDG is closely related to the GLUT-1 glucose transporter,^{39–41} and since GLUT-1 has been found to be highly overexpressed in the majority of cancers which present high [^{18}F]FDG avidity,⁴⁰ we hypothesized that GLUT-1 plays a key role in the uptake mechanism of 2GF-GNP. We further hypothesized that while the relatively large size of the 2GF-GNP (compared to that of glucose) prevents its uptake through glucose transporters, the GLUT-1 triggers a cascade of events that eventually leads to the increased uptake of the 2GF-GNP complex by cancer cells, possibly through endocytosis. Therefore, we focused our experiments on investigating the effect of GLUT-1, as well as on validating the endocytic pathway. An initial step toward investigating the internalization mechanism of 2GF-GNP was done by incubating them with A431 cells at 4 and 37 °C ($n = 3$ per group), given that endocytosis is an energy-dependent process. As demonstrated by atomic absorption spectroscopy and FACS analysis, 2GF-GNPs were internalized to a significantly lesser extent when kept at 4 °C compared to 37 °C (Figure 4A), suggesting that internalization into the cells occurs, at least partially, through an endocytic pathway. The mechanism of the remaining uptake can be attributed to diffusion. 2GF-GNP internalization into A431 cells was further verified by confocal microscopy and TEM, which clearly showed accumulation of nanoparticles inside the cells (Figure 4B). Focusing on GLUT-1, we performed a competitive experiment at high concentrations of glucose, which occupies and saturates GLUT-1 at the cell surface. In addition, we examined the effect of Cytochalasin B (CB), a well-known GLUT-1 inhibitor,^{42,43} on the cellular uptake of 2GF-GNP. As demonstrated by atomic absorption spectroscopy measurements, saturation of the medium with free glucose has significantly reduced the cellular uptake of 2GF-GNP in comparison to that obtained at lower glucose levels, by 44%

and 25%, after 20 and 120 min incubation with the 2GF-GNPs, respectively (Figure 4C). Similarly, preincubating the cells with CB has inhibited the cellular uptake of 2GF-GNPs by 44% and 28% following the same incubation times (Figure 4D). To validate that the inhibition is not due to cytotoxicity of CB, the cellular viability following CB treatment was determined using trypan blue test, showing more than 96% viability. The observed decrease in the extent of inhibition with the increasing incubation period can be attributed to the nonspecific internalization of the GNPs, which is more likely to occur during the long-period incubations. The internalization mechanism of 2GF-GNPs was further investigated with the standard fibroblast 3T3 cell line (Supplementary Figure S4). As expected, the uptake in these cells was lower than in A431 cancer cells. In addition, incubation at 4 °C as well as saturation with free glucose and preincubation with CB, have demonstrated the same trend as in A431 cells, but with lower degrees of reduction.

Altogether, these results point to a specific uptake mechanism, influenced by recognition of the glucose molecule at the GNPs surface by GLUT-1, which is overexpressed on A431 cell membranes. The interaction between GLUT-1 and the glucose coating triggers the second step of internalization, apparently through an endocytic pathway, as demonstrated by the temperature-dependent internalization.

CONCLUSIONS

In the present study, we demonstrate a novel nanoparticle-based CT imaging methodology that overcomes the main drawbacks of the currently used [¹⁸F]FDG-PET: (1) 2GF-GNP is cancer-specific and allows the distinction between cancer and inflammatory processes, (2) it offers cancer detection and imaging with no dependence on short-lived radio-tracers, and (3) it provides simultaneous anatomical and functional information using CT. In addition, unlike specific immune-targeting approaches, this imaging modality does not target the expression of one molecule, but provides unique data about the functional state of the tumor tissue.

We further showed that despite the conjugation to the GNP, the glucose molecule preserves some of its activity, allowing glucose recognition and cellular internalization, probably by receptor mediated endocytosis. In addition, we showed that due to the unique characteristics of tumor vasculatures and dissimilarities between cancer and inflammatory processes, accumulation of GNPs occurs in the tumor and not in the inflammatory lesion, thus preventing false-positive results. Future research should be done to optimize the system, such as optimization of GNPs' size which may play an important role in view of the EPR effect.

Finally, our new concept of functional CT imaging provides a new set of capabilities in cancer detection, staging and follow-up, and can be applicable to a wide range of cancers that exhibit high metabolic profiles.

METHODS

Gold Nanosphere Synthesis, Conjugation and Characterization. *Synthesis.* Synthesis of 20 nm spherical GNPs was carried out using sodium citrate as a reducing agent, based on Enüstün and Turkevich's methodology.⁴⁴ 414 μ L of 50% w/v HAuCl₄ solution were added to 200 mL purified water, and the solution was heated in an oil bath on a heating plate until boiling. Then, 4.04 mL of sodium citrate tribasic dihydrate (Sigma-Aldrich) 10% solution were added, and the solution was stirred for 10 min. After cooling to room temperature, the

solution was centrifuged until separation between nanoparticles and a redundant clear solution.

Conjugation. 120 μ L of 50 mg/mL PEG7 solution (*O*-(2-carboxyethyl)-*O'*-(2-mercaptoethyl) heptaethylene glycol) (Sigma-Aldrich) were added to the nanoparticles solution, and the solution was stirred for 4 h at room temperature. Following this step, 200 μ L of 10 mg/mL EDC solution (1-ethyl-3-(3-(dimethylamino)propyl) carbodiimide HCl) (Thermo Scientific) and 200 μ L of 10 mg/mL NHS solution (*N*-hydroxysulfosuccinimide sodium salt) (Sigma-Aldrich) were added to the nanoparticle solution. The following four glucosamine molecules were used for glucosamine conjugation: β -D-glucopyranosyl amine (Carbosynth), 2-amino-2-deoxy-D-glucose HCl (Sigma-Aldrich), 3-amino-3-deoxy-D-glucose HCl (Carbosynth) and 6-amino-6-deoxy-D-glucose HCl (Appollo Scientific). Each of these glucosamine molecules was added in excess, one at the time, resulting in four types of GF-GNPs (denoted as 1GF-GNP, 2GF-GNP, 3GF-GNP and 6GF-GNP). Centrifugation was performed until a final Au concentration of 30 mg/mL was reached.

Characterization. Transmission electron microscopy (TEM, JEM-1400, JEOL) was used to measure the size and shape of the GNPs, which were further characterized using ultraviolet–visible spectroscopy (UV–vis; UV-1650 PC; Shimadzu Corporation, Kyoto Japan), Zeta potential (ZetaSizer 3000HS; Malvern Instruments, Malvern, UK), and Dynamic light scattering (DLS) following each level of coating.

In Vitro Cell Binding Study. Human SCC A431 cells (1×10^6) were cultured in 5 mL glucose-free Dulbecco's modified Eagle's medium (DMEM) medium containing 5% FCS, 0.5% Penicillin and 0.5% Glutamine. Then, excess amounts of GNPs (four types, mentioned above) were added and incubated with cells for 30 min at 37 °C. For temperature dependence experiments, incubation of the cells with 2GF-GNPs was carried out at both 37 and 4 °C, for 30 min. In the case of incubation at 4 °C, the cells were also preincubated at 4 °C for 30 min before treatment with the GNPs. For competitive experiment with high glucose level, A431 cultures were saturated with free glucose (10 mg/mL final concentration in comparison to an original concentration of 4.5 mg/mL) for 30 min before adding the GNPs, and throughout the incubation with the GNPs. Incubation with the GNPs in this assay was for 20 and 120 min. For Cytochalasin B inhibition test, cytochalasin B (Cayman Chemical) was added to the medium (100 μ g/mL final concentration) for 2 h incubation. Then, the medium was removed and the cells were washed three times with phosphate buffered saline (PBS) before adding the GNPs. Inhibition was examined after 20 and 120 min incubation with the GNPs. Additional experiments with 3T3 cell line have been performed with the same conditions, while incubation with 2GF-GNPs was for 30 min for all assays. In all these experiments, after incubation with the GNPs the medium was washed twice with PBS, followed by trypsin treatment. The cells were centrifuged twice (7 min at 1000 rpm) in order to dispose of the unbound nanoparticles. Finally, aqua-regia was added to the cells for atomic absorption spectroscopy gold detection. Trypan blue viability test for the cells which were incubated with CB, was performed by staining the cells with 0.4% trypan blue at a dilution of 1:9 and counting using a hemocytometer. All these *in vitro* experiments were run in triplicate for each experimental group.

Confocal Microscopy Experiment. Fluorescent coated (Rhodamine B, Sigma, Israel) GF-GNPs were incubated with A431 cells for 30 min at 37 °C. The cells were subsequently washed three times in PBS prior to confocal imaging using Leica TCS SP5 with Acousto-Optical Beam Splitter microscope to acquire fluorescent and bright field images.

Sample Preparation for TEM. Four Petri dishes were seeded with 500 000 A431 human squamous cell carcinoma cells per dish. Five mL DMEM (glucose-free) was added to each dish. Cells were incubated at 37 °C for 48 h without medium replacement. Following DMEM removal, cells were fixed with 2 mL glutaraldehyde per dish. The cells were incubated for 1 h at room temperature, followed by scraping of the cells with a rubber policeman into Eppendorf tubes. Cells were then washed with Cacodylate buffer, 1% osmium, 70%, 90% and 100% alcohol washing twice, and 1:0, 3:1, 1:3 propylene oxide:AGAR washing.

Fluorescence-Activated Cell Sorter (FACS) Analysis of Nanoparticle Cellular Uptake. Cells were incubated with 2GF-GNPs for 15 min at 37 and 4 °C and then washed with PBS, followed by trypsin treatment. Then, cells were centrifuged twice (5 min in 1000 rpm) to wash out unbound nanoparticles. In the case of incubation at 4 °C, cells were kept on ice for 10 min prior to the experiment, to inhibit endocytosis, and all the solutions were precooled on ice to maintain experimental conditions strictly at 4 °C. Cells were harvested using trypsin and analyzed for cell-associated NPs using FCM scatter measurements (FACSAria III cell sorter; BD Biosciences, San Jose, CA, USA). FCM data were analyzed with the FACSDiva software (version 4.0; BD Biosciences) according to a published protocol.^{45,46} Side scatter (SSC) and forward scatter (FSC) were determined concurrently with the 488 nm blue laser, measurements were performed using a 561 nm laser with 582/15 nm filter.

Animal Model and In Vivo Experiments. In Vivo Tumor Uptake of GF-GNP. A431 cells (2×10^6) were injected subcutaneously into the back flank area of nude mice aged 6 weeks. When the tumor reached a diameter of 4–5 mm, the four types of GF-GNPs (200 μ L, 30 mg/mL) were intravenously injected into their tail vein (5 mice per group). Experimental procedure was identical for all four GF-GNP types. At 3.5 h post IV injection, the animals were scanned by micro-CT scanner and then sacrificed. Gold concentration in the tumor and major organs (kidney, liver, spleen and plasma (data not shown) was quantitatively measured by atomic absorption spectroscopy.

Differentiation between Tumor and Inflammation. Human SCC xenografts and inflammation were established in 14 mice. First, mice were inoculated subcutaneously in the left hind leg with 2×10^6 SCC-A431 cells. Once the tumor reached the appropriate size of 4–5 mm, inflammation was established in the back, posterior to the lungs, by a subcutaneous injection of 100 μ L of turpentine oil. Four days post turpentine injection, [¹⁸F]FDG (5.2 ± 0.2 MBq) was IV injected into four mice, and 1 h dynamic PET acquisitions were started concomitant to the IV injection. In addition, 2GF-GNPs were IV injected to all mice. CT scans were performed before injection and at 3.5 h post injection. Then, mice were sacrificed and gold concentration was quantitatively measured in the tumor and within the inflammatory lesion by atomic absorption spectroscopy.

CT Analysis. CT scans were performed using a micro-CT scanner (Skyscan High Resolution Model 1176) with nominal resolution of 35 μ m, 0.2 mm aluminum filter, and tube voltage of 45 kV. Reconstruction was done with a modified Feldkamp⁴⁷ algorithm using the SkyScanNRecon software accelerated by GPU.⁴⁸ Ring artifact reduction, Gaussian smoothing (3%), and beam hardening correction (20%) were applied. Volume rendered three-dimensional (3D) images were generated using an RGBA transfer function in SkyScan CT-Volume ("CTVol") software and in SkyScan CT-Voxel ("CTVox") software.

[¹⁸F]FDG-PET/CT. Mice were anesthetized with isoflurane (1% – 2.5% in O₂) and maintained normothermic using a heating pad. Following a CT attenuation-correction scan, PET acquisitions were carried out in list-mode using an Inveon MM PET-CT small animal-dedicated scanner (Siemens Medical Solutions, USA). [¹⁸F]FDG was injected IV through the lateral tail-vein, and 1 h dynamic PET acquisitions were started concomitant to the IV injection. Emission sinograms were normalized and corrected for attenuation, scatter, randoms, dead time and decay. Image reconstruction was performed using Fourier rebinning and two-dimensional ordered-subsets expectation maximization (2D-OSEM), with a voxel size of $0.776 \times 0.776 \times 0.796$ mm³. Image analysis and quantification of [¹⁸F]FDG concentration in the tumor and inflammatory lesion were done using Inveon Research Workplace 4.2 (Siemens).

Atomic Absorption Spectroscopy Analysis. Atomic absorption spectroscopy (AA 140; Agilent Technologies, Santa Clara, CA) was used to determine amounts of gold in the investigated samples. Cell samples from the *in vitro* experiments were dissolved in 100 μ L aqua regia acid (a mixture of nitric acid and hydrochloric acid in a volume ratio of 1:3) and diluted with purified water to a total volume of 4 mL. For the *in vivo* experiment, dissected tissues were melted with 1 mL aqua regia acid and then evaporated and diluted to a total volume of 4

mL. After filtration of the samples, gold concentrations were determined according to absorbance values, with correlation to calibration curves, constructed from solution with known gold concentrations.

ASSOCIATED CONTENT

Supporting Information

The Supporting Information is available free of charge on the ACS Publications website at DOI: 10.1021/acsnano.5b07576.

Characterization of GF-GNPs: TEM, UV–vis, Zeta potential and DLS; Confocal images of A431 cells after incubation with GF-GNPs; Biodistribution of 2GF-GNP; Internalization mechanism study in 3T3 cell line. (PDF)

AUTHOR INFORMATION

Corresponding Author

*E-mail: rachela.popovtzer@biu.ac.il.

Author Contributions

#M.M. and T.D. contributed equally to this work.

Notes

The authors declare no competing financial interest.

ACKNOWLEDGMENTS

This work was partially supported by the Research and Development Chief Scientist Kamin grant (49544), by the Israel Cancer Research Fund (ICRF), by the Israel Science Foundation grant (749/14), and by the doctoral scholarship for applicable and scientific engineering research, granted to Tamar Dreifuss and Oshra Betzer by the Ministry of Science, Technology & Space, Israel.

REFERENCES

- (1) Strauss, L. G. Fluorine-18 Deoxyglucose and False-Positive Results: A Major Problem in the Diagnostics of Oncological Patients. *Eur. J. Nucl. Med.* **1996**, *23*, 1409–1415.
- (2) Kostakoglu, L.; Agress, H.; Goldsmith, S. J. Clinical Role of FDG PET in Evaluation of Cancer Patients. *Radiographics* **2003**, *23*, 315–340 quiz 533.
- (3) Lusic, H.; Grinstaff, M. W. X-Ray-Computed Tomography Contrast Agents. *Chem. Rev.* **2013**, *113*, 1641–1666.
- (4) Meir, R.; Motiei, M.; Popovtzer, R. Gold Nanoparticles for *in Vivo* Cell Tracking. *Nanomedicine (London, U. K.)* **2014**, *9*, 2059–2069.
- (5) Shilo, M.; Sharon, A.; Baranes, K.; Motiei, M.; Lellouche, J.-P. M.; Popovtzer, R. The Effect of Nanoparticle Size on the Probability to Cross the Blood-Brain Barrier: An *in-Vitro* Endothelial Cell Model. *J. Nanobiotechnol.* **2015**, *13*, 19.
- (6) Arvizo, R.; Bhattacharya, R.; Mukherjee, P. Gold Nanoparticles: Opportunities and Challenges in Nanomedicine. *Expert Opin. Drug Delivery* **2010**, *7*, 753.
- (7) Hainfeld, J. F.; Slatkin, D. N.; Focella, T. M.; Smilowitz, H. M. Gold Nanoparticles: A New X-Ray Contrast Agent. *Br. J. Radiol.* **2006**, *79*, 248–253.
- (8) Betzer, O.; Shwartz, A.; Motiei, M.; Kazimirsky, G.; Gispan, I.; Damti, E.; Brodie, C.; Yadid, G.; Popovtzer, R. Nanoparticle-Based CT Imaging Technique for Longitudinal and Quantitative Stem Cell Tracking within the Brain: Application in Neuropsychiatric Disorders. *ACS Nano* **2014**, *8*, 9274–9285.
- (9) Meir, R.; Shamalov, K.; Betzer, O.; Motiei, M.; Horovitz-Fried, M.; Yehuda, R.; Popovtzer, A.; Popovtzer, R.; Cohen, C. J. Nanomedicine for Cancer Immunotherapy: Tracking Cancer-Specific T-Cells *in Vivo* with Gold Nanoparticles and CT Imaging. *ACS Nano* **2015**, *9*, 6363–6372.
- (10) Rand, D.; Ortiz, V.; Liu, Y.; Derdak, Z.; Wands, J. R.; Tatíček, M.; Rose-Petrucci, C. Nanomaterials for X-Ray Imaging: Gold

Nanoparticle Enhancement of X-Ray Scatter Imaging of Hepatocellular Carcinoma. *Nano Lett.* **2011**, *11*, 2678–2683.

(11) Dreifuss, T.; Betzer, O.; Shilo, M.; Popovtzer, A.; Motiei, M.; Popovtzer, R. A Challenge for Theranostics: Is the Optimal Particle for Therapy Also Optimal for Diagnostics? *Nanoscale* **2015**, *7*, 15175–15184.

(12) Lukianova-Hleb, E. Y.; Anderson, L. J. E.; Lee, S.; Hafner, J. H.; Lapotko, D. O. Hot Plasmonic Interactions: A New Look at the Photothermal Efficacy of Gold Nanoparticles. *Phys. Chem. Chem. Phys.* **2010**, *12*, 12237–12244.

(13) Jakobsohn, K.; Motiei, M.; Sinvani, M.; Popovtzer, R. Towards Real-Time Detection of Tumor Margins Using Photothermal Imaging of Immune-Targeted Gold Nanoparticles. *Int. J. Nanomed.* **2012**, *7*, 4707–4713.

(14) Cho, W.-S.; Cho, M.; Jeong, J.; Choi, M.; Han, B. S.; Shin, H.-S.; Hong, J.; Chung, B. H.; Jeong, J.; Cho, M.-H. Size-Dependent Tissue Kinetics of PEG-Coated Gold Nanoparticles. *Toxicol. Appl. Pharmacol.* **2010**, *245*, 116–123.

(15) De Jong, W. H.; Hagens, W. I.; Krystek, P.; Burger, M. C.; Sips, A. J. a M.; Geertsma, R. E. Particle Size-Dependent Organ Distribution of Gold Nanoparticles after Intravenous Administration. *Biomaterials* **2008**, *29*, 1912–1919.

(16) Villiers, C.; Freitags, H.; Couderc, R.; Villiers, M.-B.; Marche, P. Analysis of the Toxicity of Gold Nano Particles on the Immune System: Effect on Dendritic Cell Functions. *J. Nanopart. Res.* **2010**, *12*, 55–60.

(17) Betzer, O.; Meir, R.; Dreifuss, T.; Shamalov, K.; Motiei, M.; Schwartz, A.; Baranes, K.; Cohen, C. J.; Shraga-Heled, N.; Ofir, R.; Yadid, G.; Popovtzer, R. *In-Vitro* Optimization of Nanoparticle-Cell Labeling Protocols for *In-Vivo* Cell Tracking Applications. *Sci. Rep.* **2015**, *5*, 15400.

(18) Popovtzer, A.; Mizrachi, A.; Motiei, M.; Bragilovski, D.; Lubimov, L.; Levi, M.; Hilly, O.; Ben-Aharon, I.; Popovtzer, R. Actively Targeted Gold Nanoparticles as Novel Radiosensitizer Agents: An *in Vivo* Head and Neck Cancer Model. *Nanoscale* **2016**, *8*, 2–9.

(19) McDonald, D. M.; Baluk, P. Imaging of Angiogenesis in Inflamed Airways and Tumors: Newly Formed Blood Vessels Are Not Alike and May Be Wildly Abnormal: Parker B. Francis Lecture. *Chest* **2005**, *128*, 602S–608S.

(20) Maeda, H.; Nakamura, H.; Fang, J. The EPR Effect for Macromolecular Drug Delivery to Solid Tumors: Improvement of Tumor Uptake, Lowering of Systemic Toxicity, and Distinct Tumor Imaging *in Vivo*. *Adv. Drug Delivery Rev.* **2013**, *65*, 71–79.

(21) Maeda, H. Tumor-Selective Delivery of Macromolecular Drugs via the EPR Effect: Background and Future Prospects. *Bioconjugate Chem.* **2010**, *21*, 797–802.

(22) Maeda, H. The Link between Infection and Cancer: Tumor Vasculature, Free Radicals, and Drug Delivery to Tumors via the EPR Effect. *Cancer Sci.* **2013**, *104*, 779–789.

(23) Li, W.; Szoka, F. C. Lipid-Based Nanoparticles for Nucleic Acid Delivery. *Pharm. Res.* **2007**, *24*, 438–449.

(24) Baluk, P.; Hashizume, H.; McDonald, D. M. Cellular Abnormalities of Blood Vessels as Targets in Cancer. *Curr. Opin. Genet. Dev.* **2005**, *15*, 102–111.

(25) McDonald, D. M.; Choyke, P. L. Imaging of Angiogenesis: From Microscope to Clinic. *Nat. Med.* **2003**, *9*, 713–725.

(26) Hashizume, H.; Baluk, P.; Morikawa, S.; McLean, J. W.; Thurston, G.; Roberge, S.; Jain, R. K.; McDonald, D. M. Openings between Defective Endothelial Cells Explain Tumor Vessel Leakiness. *Am. J. Pathol.* **2000**, *156*, 1363–1380.

(27) Fang, J.; Nakamura, H.; Maeda, H. The EPR Effect: Unique Features of Tumor Blood Vessels for Drug Delivery, Factors Involved, and Limitations and Augmentation of the Effect. *Adv. Drug Delivery Rev.* **2011**, *63*, 136–151.

(28) Maeda, H.; Matsumura, Y. Tumorotropic and Lymphotropic Principles of Macromolecular Drugs. *Crit. Rev. Ther. Drug Carrier Syst.* **1989**, *6*, 193–210.

(29) Maeda, H. SMANCS and Polymer-Conjugated Macromolecular Drugs: Advantages in Cancer Chemotherapy. *Adv. Drug Delivery Rev.* **2001**, *46*, 169–185.

(30) Maeda, H.; Fang, J.; Inutsuka, T.; Kitamoto, Y. Vascular Permeability Enhancement in Solid Tumor: Various Factors, Mechanisms Involved and Its Implications. *Int. Immunopharmacol.* **2003**, *3*, 319–328.

(31) Maeda, H.; Seymour, L. W.; Miyamoto, Y. Conjugates of Anticancer Agents and Polymers: Advantages of Macromolecular Therapeutics *in Vivo*. *Bioconjugate Chem.* **1992**, *3*, 351–362.

(32) Sawa, T.; Sahoo, S.; Maeda, H. Water-Soluble Polymer Therapeutics with Special Emphasis on Cancer Chemotherapy. *Polymeric Biomaterials, the PBM Series 1*; 2002, pp 233–266.

(33) Reuveni, T.; Motiei, M.; Romman, Z.; Popovtzer, A.; Popovtzer, R. Targeted Gold Nanoparticles Enable Molecular CT Imaging of Cancer: An *in Vivo* Study. *Int. J. Nanomed.* **2011**, *6*, 2859.

(34) Zhang, G.; Yang, Z.; Lu, W.; Zhang, R.; Huang, Q.; Tian, M.; Li, L.; Liang, D.; Li, C. Influence of Anchoring Ligands and Particle Size on the Colloidal Stability and *in Vivo* Biodistribution of Polyethylene Glycol-Coated Gold Nanoparticles in Tumor-Xenografted Mice. *Biomaterials* **2009**, *30*, 1928–1936.

(35) Mueckler, M.; Makepeace, C. Analysis of Transmembrane Segment 8 of the GLUT1 Glucose Transporter by Cysteine-Scanning Mutagenesis and Substituted Cysteine Accessibility. *J. Biol. Chem.* **2004**, *279*, 10494–10499.

(36) Barnett, J. E.; Holman, G. D.; Munday, K. A. Structural Requirements for Binding to the Sugar-Transport System of the Human Erythrocyte. *Biochem. J.* **1973**, *131*, 211–221.

(37) McLarty, K.; Moran, M. D.; Scollard, D. A.; Chan, C.; Sabha, N.; Mukherjee, J.; Guha, A.; McLaurin, J.; Nitz, M.; Houle, S.; Wilson, A. A.; Reilly, R. M.; Vasdev, N. Comparisons of [¹⁸F]-1-Deoxy-1-Fluoro-Scyllo-Inositol with [¹⁸F]-FDG for PET Imaging of Inflammation, Breast and Brain Cancer Xenografts in Athymic Mice. *Nucl. Med. Biol.* **2011**, *38*, 953–959.

(38) Liu, R.-S.; Chou, T.-K.; Chang, C.-H.; Wu, C.-Y.; Chang, C.-W.; Chang, T.-J.; Wang, S.-J.; Lin, W.-J.; Wang, H.-E. Biodistribution, Pharmacokinetics and PET Imaging of [(18)F]FMISO, [(18)F]FDG and [(18)F]FAC in a Sarcoma- and Inflammation-Bearing Mouse Model. *Nucl. Med. Biol.* **2009**, *36*, 305–312.

(39) Brown, R. S.; Leung, J. Y.; Kison, P. V.; Zasadny, K. R.; Flint, a; Wahl, R. L. Glucose Transporters and FDG Uptake in Untreated Primary Human Non-Small Cell Lung Cancer. *J. Nucl. Med.* **1999**, *40*, 556–565.

(40) Higashi, K.; Ueda, Y.; Sakurai, A.; Mingwang, X.; Xu, L.; Murakami, M.; Seki, H.; Oguchi, M.; Taki, S.; Nambu, Y.; Tonami, H.; Katsuda, S.; Yamamoto, I. Correlation of Glut-1 Glucose Transporter Expression with [(18)F]FDG Uptake in Non-Small Cell Lung Cancer. *Eur. J. Nucl. Med.* **2000**, *27*, 1778–1785.

(41) Kato, H.; Takita, J.; Miyazaki, T.; Nakajima, M.; Fukai, Y.; Masuda, N.; Fukuchi, M.; Manda, R.; Ojima, H.; Tsukada, K.; Kuwano, H.; Oriuchi, N.; Endo, K. Correlation of 18-F-Fluorodeoxyglucose (FDG) Accumulation with Glucose Transporter (Glut-1) Expression in Esophageal Squamous Cell Carcinoma. *Anticancer Res.* **2003**, *23*, 3263–3272.

(42) Gottschalk, I.; Lundqvist, A.; Zeng, C.-M.; Häggglund, C. L.; Zuo, S.-S.; Brekkan, E.; Eaker, D.; Lundahl, P. Conversion between Two Cytochalasin B-Binding States of the Human GLUT1 Glucose Transporter. *Eur. J. Biochem.* **2000**, *267*, 6875–6882.

(43) Pinkofsky, H. B.; Dwyer, D. S.; Bradley, R. J. The Inhibition of GLUT1 Glucose Transport and Cytochalasin B Binding Activity by Tricyclic Antidepressants. *Life Sci.* **1999**, *66*, 271–278.

(44) Enustun, B. V.; Turkevich, J. Coagulation of Colloidal Gold. *J. Am. Chem. Soc.* **1963**, *85*, 3317–3328.

(45) Melzer, S.; Ankri, R.; Fixler, D.; Tarnok, A. Nanoparticle Uptake by Macrophages in Vulnerable Plaques for Atherosclerosis Diagnosis. *J. Biophotonics* **2015**, *8*, 871–883.

(46) Ankri, R.; Melzer, S.; Tarnok, A.; Fixler, D. Detection of Gold Nanorods Uptake by Macrophages Using Scattering Analyses Combined with Diffusion Reflection Measurements as a Potential

Tool for *in Vivo* Atherosclerosis Tracking. *Int. J. Nanomed.* **2015**, *10*, 4437–4446.

(47) Feldkamp, L. A.; Davis, L. C.; Kress, J. W. Practical Cone-Beam Algorithm. *J. Opt. Soc. Am. A* **1984**, *1*, 612.

(48) Yan, G.; Tian, J.; Zhu, S.; Dai, Y.; Qin, C. Fast Cone-Beam CT Image Reconstruction Using GPU Hardware. *J. X-ray Sci. Technol.* **2008**, *16*, 225–234.

(49) Almeida, J. P. M.; Chen, A. L.; Foster, A.; Drezek, R. *In Vivo* Biodistribution of Nanoparticles. *Nanomedicine (London, U. K.)* **2011**, *6*, 815–835.

(50) Li, S.-D.; Huang, L. Pharmacokinetics and Biodistribution of Nanoparticles. *Mol. Pharmaceutics* **2008**, *5*, 496–504.